nature portfolio

https://doi.org/10.1038/s41567-022-01743-4

Supplementary information

Topological semimetal driven by strong correlations and crystalline symmetry

In the format provided by the authors and unedited

Supplementary Information for "Topological Semimetal Driven by Strong Correlations and Crystalline Symmetry"

Lei Chen[1], Chandan Setty[1], Haoyu Hu[1], Maia G. Vergniory[2,3], Sarah E. Grefe[4], Lukas Fischer[5], Xinlin Yan[5], Gaku Eguchi[5], Andrey Prokofiev[5], Silke Paschen[5,1,*], Jennifer Cano[6,7,*], and Qimiao Si[1,*]

[1]Department of Physics and Astronomy, Rice Center for Quantum Materials, Rice University, Houston, Texas 77005, USA

[2]Max Planck Institute for Chemical Physics of Solids, Noethnitzer Str. 40, 01187 Dresden, Germany

[3]Donostia International Physics Center, P. Manuel de Lardizabal 4, 20018 Donostia-San Sebastian, Spain

[4]Theoretical Division, Los Alamos National Laboratory, Los Alamos, New Mexico 87545, USA

[5]Institute of Solid State Physics, Vienna University of Technology, Wiedner Hauptstr. 8-10, 1040 Vienna, Austria

[6]Department of Physics and Astronomy, Stony Brook University, Stony Brook, NY 11794, USA

[7]Center for Computational Quantum Physics, Flatiron Institute, New York, NY 10010, USA

[*]Corresponding authors; emails:
qmsi@rice.edu; jennifer.cano@stonybrook.edu; paschen@ifp.tuwien.ac.at

Kondo-driven topological semimetals in 2D

The Kondo effect leads to composite fermions near the Fermi energy. For the inversion-symmetric case ($\Delta = 0$), the renormalized dispersion as shown in Fig. S1(a) was already discussed in the main text. For the case with broken inversion symmetry (i.e., with nonzero Δ), we show the renormalized dispersion in Fig. S1(b). The four-fold degenerate states at X and Y are split into two pairs of two-fold Weyl nodes above and below the Fermi energy. The different branches of the Weyl nodes cross each other at the Fermi energy, giving rise to Fermi-energy-bound Weyl-nodal lines, as shown in Fig. S1(c). The Weyl-nodal lines are protected by the mirror nonsymmorphic symmetry[1,2]. We note that, here too, the Kondo-driven nodal lines have been identified in the presence of SOC.

Kondo-driven topological semimetals for SG 129

Utilizing the 2D model as the building block, we consider how the Kondo-driven topological nodes

develop in the SG 129 case. This can already be done with a direct stacking along the z-direction. As shown in Fig. S2(a), the symmetry enforced Dirac points at high symmetry points in 2D is extended along z-direction and becomes Dirac nodal lines along the high symmetry hinges; the degree of their dispersion is related to the strength of the z-direction hoppings. Thus, there could only be Dirac points that cross the Fermi energy [Fig. S2(b)]. In the presence of a ferromagnetic order or Zeeman coupling from an external magnetic field, the Dirac nodes are turned into Weyl nodes. In addition, pairs of Weyl nodes can in principle appear along $\Gamma - X/Y/Z$, which are protected by rotational symmetries according to magnetic group analysis. This is illustrated in Fig. S2(c)(d), which show a pair of Weyl nodes along $\Gamma - Z$.

Additional data for the Kondo-driven nodal line in 3D

In Fig. 3 of the main text, we showed the renormalized electronic structure for the 3D square net along high-symmetry directions within the $k_z = 0$ plane. Here, we plot the bands along high-symmetry directions in the entire 3D Brillouin zone. The renormalized band structure is shown in Fig. S3(a) along the path connecting high symmetry points as can be seen through Fig. S3(b). Except for the Weyl line in the $k_z = 0$ plane, the heavy bands are fully gapped across the 3D Brillouin zone.

Hamiltonians in matrix form

Consider first the 2D case. The Hamiltonian of the conduction c-fermion, $\mathcal{H}_c$, is described in a matrix form: $\mathcal{H}_c = \sum_{\mathbf{k}} \Psi^\dagger_{\mathbf{k}} H_c(\mathbf{k}) \Psi_{\mathbf{k}}$, where $\Psi^T_{\mathbf{k}} = (c_{\mathbf{k}\uparrow A}, c_{\mathbf{k}\downarrow A}, c_{\mathbf{k}\uparrow B}, c_{\mathbf{k}\downarrow B})$, with A and B being the two sublattices, $\mathbf{k}$ the wavevector, and $\sigma = \uparrow, \downarrow$ marking the spin quantum numbers.

$$H_c(\mathbf{k}) = \begin{pmatrix} f_2(\mathbf{k}) & f_{SO}(\mathbf{k}) & f_1(\mathbf{k}) + f_\Delta(\mathbf{k}) & 0 \\ f_{SO}(\mathbf{k}) & f_2(\mathbf{k}) & 0 & f_1(\mathbf{k}) - f_\Delta(\mathbf{k}) \\ f_1(\mathbf{k}) + f_\Delta(\mathbf{k}) & 0 & f_2(\mathbf{k}) & -f_{SO}(\mathbf{k}) \\ 0 & f_1(\mathbf{k}) - f_\Delta(\mathbf{k}) & -f_{SO}(\mathbf{k}) & f_2(\mathbf{k}) \end{pmatrix},$$

with

$$\begin{aligned} f_1(\mathbf{k}) &= t_1 \cos\frac{k_x}{2} \cos\frac{k_y}{2}\,, \\ f_2(\mathbf{k}) &= t_2(\cos k_x + \cos k_y)\,, \\ f_{SO}(\mathbf{k}) &= t^{SO}(-\sin k_y - i \sin k_x)\,, \\ f_\Delta(\mathbf{k}) &= \Delta \sin(\frac{k_x - k_y}{2})\,, \end{aligned}$$

where t_1/t_2 are the nearest and next-nearest neighbor hopping parameters, t^{SO} is the symmetry-allowed SOC and Δ breaks the inversion symmetry.

Consider next the Hamiltonian for the 3D model. For the conduction c-fermions, the Hamiltonian now takes the form:

$$\mathcal{H}_c^{3D} = \sum_{\mathbf{k}} \Phi_{\mathbf{k}}^\dagger H_c^{3D}(\mathbf{k}) \Phi_{\mathbf{k}} \,,$$

where $\Phi_{\mathbf{k}}^T = (c^s_{\mathbf{k}\uparrow A}, c^s_{\mathbf{k}\downarrow A}, c^s_{\mathbf{k}\uparrow B}, c^s_{\mathbf{k}\downarrow B}, c^p_{\mathbf{k}\uparrow A}, c^p_{\mathbf{k}\downarrow A}, c^p_{\mathbf{k}\uparrow B}, c^p_{\mathbf{k}\downarrow B})$. And

$$H_c^{3D}(\mathbf{k}) = \begin{pmatrix} H_c(k_x,k_y) + H_z(k_z) & \rho(k_z) \\ \rho^\dagger(k_z) & -H_c(k_x,k_y) - H_z(k_z) \end{pmatrix} \,,$$

where

$$H_z(k_z) = (\Delta_z + t_z^2 \cos k_z) \mathbb{1}_{4\times 4} \,,$$

and

$$\rho(k_z) = \begin{pmatrix} -it_z^1 \sin\frac{k_z}{2} & & & -im_z \\ & -it_z^1 \sin\frac{k_z}{2} & -im_z & \\ & -im_z & -it_z^1 \sin\frac{k_z}{2} & \\ -im_z & & & -it_z^1 \sin\frac{k_z}{2} \end{pmatrix} .$$

Here, Δ_z is the chemical potential difference between two layers, t_z^1/t_z^2 represent the nearest- and next-nearest-neighbor hoppings along the z-direction and m_z is the SOC along z-direction.

Saddle point equations

We describe the auxiliary-boson method in this section. In the 2D square-net model, we first fix the electron filling to be one per site

$$n_d + n_c = 1 \,, \tag{S1}$$

with

$$n_d = \tfrac{1}{N_\mathrm{u}} \textstyle\sum_{i,\sigma} d_{i\sigma}^\dagger d_{i\sigma} \,, \tag{S2}$$

$$n_c = \tfrac{1}{N_\mathrm{u}} \textstyle\sum_{i,\sigma} c_{i\sigma}^\dagger c_{i\sigma} \,, \tag{S3}$$

where N_u counts the total number of sites.

In the infinite-U limit, the localized d-electrons can be represented as $d_{i\sigma}^\dagger = b_i f_{i\sigma}^\dagger$ with local constraint

$$b_i^\dagger b_i + \sum_\sigma f_{i\sigma}^\dagger f_{i\sigma} = 1 \,. \tag{S4}$$

This constraint rules out the double occupancy entirely. At the saddle point, the auxiliary bosons condense, with $b_i \to \langle b_i \rangle = r$. We further introduce a uniform Lagrangian multiplier l to enforce

the local constraint in Eq. S4, which gives rise to the saddle-point Hamiltonian:

$$\mathcal{H}_s = \mathcal{H} + l\left(\frac{1}{N_{\rm u}}\sum_{i,\sigma} f^\dagger_{i\sigma} f_{i\sigma} + r^2 - 1\right) - \mu\,\frac{1}{N_{\rm u}}\sum_{i,\sigma} n^c_{i\sigma}\,, \tag{S5}$$

where μ is the chemical potential. The saddle point equations are

$$\sum_\sigma \left(V\langle c^\dagger_\sigma f_\sigma\rangle + h.c.\right) - 2rl = 0\,, \tag{S6}$$

$$\sum_\sigma \langle f^\dagger_\sigma f_\sigma\rangle - r^2 = 1\,. \tag{S7}$$

Together with the filling constraint Eq. S1, we can self-consistently determine the variational parameters (μ, r, l).

We apply the same auxiliary-boson method to the 3D stacked square net with a saddle-point Hamiltonian

$$\begin{aligned} H = {} & H_c^{3D} + r_1 V\frac{1}{N_u}\sum_{i,\sigma}(s^\dagger_{i,\sigma} f^1_{i,\sigma} + h.c.) + E_d\frac{1}{N_u}\sum_{i,\sigma} f^{1\dagger}_{i,\sigma} f^1_{i,\sigma} \\ & + r_2 V\frac{1}{N_u}\sum_{i,\sigma}(p^\dagger_{i,\sigma} f^2_{i,\sigma} + h.c.) + E_d\frac{1}{N_u}\sum_{i,\sigma} f^{2\dagger}_{i,\sigma} f^2_{i,\sigma} \\ & + l_1\frac{1}{N_u}\left(\sum_{i,\sigma} f^{1\dagger}_{i,\sigma} f^1_{i,\sigma} + r_1^2 - 1\right) + l_2\frac{1}{N_u}\left(\sum_{i,\sigma} f^{2\dagger}_{i,\sigma} f^2_{\sigma} + r_2^2 - 1\right) \\ & - \mu\frac{1}{N_u}\sum_{i,\sigma}\left(s^\dagger_{i,\sigma} s_{i,\sigma} + p^\dagger_{i,\sigma} p_{i,\sigma}\right)\,, \end{aligned} \tag{S8}$$

where f^1_σ and f^2_σ, r_1 and r_2, l_1 and l_2 represent the auxiliary fermions, condensed auxiliary bosons and Lagrangian multipliers for each layer.

The saddle point equations are

$$\frac{1}{N_u}\sum_\sigma \left(V\langle s^\dagger_\sigma f^1_\sigma\rangle + h.c.\right) - 2r_1 l_1 = 0\,, \tag{S9}$$

$$\frac{1}{N_u}\sum_\sigma \langle f^{1\dagger}_\sigma f^1_\sigma\rangle - r_1^2 = 1\,, \tag{S10}$$

$$\frac{1}{N_u}\sum_\sigma \left(V\langle p^\dagger_\sigma f^2_\sigma\rangle + h.c.\right) - 2r_2 l_2 = 0\,, \tag{S11}$$

$$\frac{1}{N_u}\sum_\sigma \langle f^{2\dagger}_\sigma f^2_\sigma\rangle - r_2^2 = 1\,. \tag{S12}$$

The filling is still fixed to be one per site.

Symmetry analysis of the interacting Green's function

We briefly note on the symmetry analysis of the interacting Green's function[3]. This utilizes the

eigenvectors and eigenfunctions of the single-particle Green's function of an interacting multi-band system. The symmetry analysis as applied on the eigenvectors proceeds in a similar way as for the Bloch functions of noninteracting bands. The degeneracies of the eigenvectors imply the degeneracies of the peaks in the energy dispersion of the corresponding spectral function. Further details can be found in Ref. 3.

Search for new materials to realize the proposed topological semimetal phases driven by strong correlations

The search for candidate materials started with the retrieval of Ce compounds crystallizing in the space group P4/nmm (SG 129) from the Inorganic Crystal Structure Database (ICSD). Multiple entries were unified. Only materials containing Ce atoms in the unique 2c Wyckoff position were taken into account. This yields 142 chemical compounds as specified in Fig. 4(a). In the second step, the following entries were removed: Insulators (oxides, oxohalogenides, oxosulfides), off-stoichiometric phases and solid solutions, obviously good metals (based on valence considerations) and superconductors and related phases. The remaining 39 pure stoichiometric phases were predominantly ternary cerium compounds of pnictogens, chalcogens, and the silicon group elements [Fig. S4(a)]. The further selection has to be done by literature search and inspection of the measured physical properties (where available), as illustrated in the next subsection. Two examples resulting from such a search are identified as strongly correlated paramagnetic semimetals, $CePt_2Si_2$ and $CeRh_2Ga_2$, and are proposed as materials for the correlation-driven topological semimetal phases advanced here. A similar procedure applies to the case of SG 31 with Ce atoms. The 4 materials of this case are shown in Fig. S4(b).

We note in passing that magnetic materials are also of interest, even though they are not the focus of the present work. For example, in the case of SG 129, CeSbTe is a well-known material that hosts f-electrons[4]. However, it exhibits an antiferromagnetic order at $T_N = 2.7$ K, which breaks time-reversal symmetry. Still, the amount of entropy that has been measured in such a temperature range suggests that the system will be strongly correlated if it is tuned to a paramagnetic state. Thus, tuning these systems into their paramagnetic ground state is suggested as a means of realizing the Kondo-driven topological semimetal we have advanced here.

$CeRh_2Ga_2$ and $CePt_2Si_2$ as strongly correlated semimetals

The two candidate materials we have identified, $CeRh_2Ga_2$ and $CePt_2Si_2$, show properties that are characteristic of strongly correlated semimetals. Their strong correlations are signaled by the large enhancement of the specific heat from the typical values of weakly correlated metals.

The electronic specific-heat coefficient C/T reaches 130 and 80 mJ/mol K^2, respectively[5,6] (*i.e.* about 100 times the effective mass of weakly correlated bulk metals). Their semimetal nature is captured by the resistivity as a function of temperature, respectively shown in Fig. S5(a)(b) for the two compounds[5,7], which behaves similarly as Fig. S5(c)(d), respectively, for the well-established heavy-fermion semimetals $Ce_3Bi_4Pd_3$ and CeNiSn[8,9]. In all cases, the temperature dependence of the resistivity is neither activated, as a fully-gapped system would be, nor showing a giant T^2-dependent component at low temperatures with a positive temperature slope, as a typical heavy-fermion metal would be. This feature is accompanied by the relatively large magnitude of the resistivity.

Further details and additional results of the DFT calculations

The electronic structure calculations were performed using the Vienna ab initio simulation package (VASP)[10,11] with the Perdew, Burke and Ernz-erhof (PBE) generalized gradient approximation for the exchange correlation potential[12]. The f states were removed from the pseudo-potential to model the band structure. The interaction between the ion cores and valence electrons was described by the projector augmented-wave method[13]. The Hamiltonian contained the scalar relativistic corrections, and the SOC was taken into account by the second variation method[14].

The calculation for $CeRh_2Ga_2$ is in principle more difficult, given that the Rh- and Ga-site displacive disorder in the existing materials has been reported[15]. To get a qualitative understanding, we have carried out f-core DFT calculations but ignoring the disorder, with the Rh and Ga atoms fully assigned to the 2c and 2a sites, respectively. The results are shown in Fig. S7.

A realistic periodic Anderson lattice model can be constructed as follows. One can start from a tight-binding representation for the conduction electrons based on the understanding of the dominant orbitals that form the spd conduction-electron bands; to illustrate the latter, we have analysed the atomic and orbital contents in the case of $CePt_2Si_2$, finding the dominating contributions to come from the Pt d- and s-orbitals (Fig. S8). One also needs to determine the lowest Kramers doublet for the f-electrons, which is an interacting problem; in practice, this usually requires input from spectroscopic measurements. Thereafter, one can construct the hybridization matrix.

Specific heat

To calculate the low-T specific heat, we focus on the linear-dispersion regime where we can approximate the dispersion $\epsilon_{\mathbf{k}} = \epsilon_{\mathbf{k}_\perp} = \hbar v^* k_\perp$. Here, $\mathbf{k} = (k_\parallel, \mathbf{k}_\perp)$ represents the decomposition of the wave vector into the components parallel and perpendicular to the nodal line; $\mathbf{k}_\perp$ itself has two

components.

The specific heat becomes

$$\begin{aligned} c_v &= \frac{\partial}{\partial T}\int_{\infty}^{+\infty}\frac{d\epsilon}{(2\pi)^3}\epsilon\rho(\epsilon)f(\epsilon) \\ &= \frac{\partial}{\partial T}\int_{-\infty}^{+\infty}\frac{d\epsilon}{(2\pi)^3}\epsilon\frac{2K\pi\epsilon}{(\hbar v^*)^2}\frac{1}{e^{\epsilon/k_BT}+1} \\ &= \frac{K}{(2\pi)^3}\frac{\partial}{\partial T}\int_0^{2\pi}d\theta\int_0^{k_K}dk_\perp\frac{2\pi(\hbar v^*)^3k_\perp^2}{(\hbar v)^2}\frac{1}{e^{\hbar v^*k_\perp/k_BT}+1} \\ &= \frac{K}{2\pi}\frac{9\zeta(3)}{2}k_B\left(\frac{k_BT}{\hbar v^*}\right)^2, \end{aligned} \tag{S13}$$

where K is the length of the nodal line and $\zeta(3)\approx 1.202$. So the specific heat per unit volume is

$$c_v = \Gamma\, T^2\,, \tag{S14}$$

$$\Gamma = \tfrac{K}{2\pi}\tfrac{9\zeta(3)}{2}\tfrac{(k_B)^3}{(\hbar v^*)^2}\,. \tag{S15}$$

1. Young, S. M. & Kane, C. L. Dirac semimetals in two dimensions. *Phys. Rev. Lett.* **115**, 126803 (2015).
2. Wu, W., Jiao, Y., Li, S., Sheng, X.-L., Yu, Z.-M. & Yang, S. A. Hourglass Weyl loops in two dimensions: Theory and material realization in monolayer GaTeI family. *Phys. Rev. Materials* **3**, 054203 (2019).
3. Hu, H., Chen, L., Setty, C., Grefe, S. E., Prokofiev, A., Kirchner, S., Paschen, S., Cano, J. & Si, Q. Gapless electronic topology without free-electron counterpart. *arXiv:2110.06182* (2021).
4. Schoop, L. M., Topp, A., Lippmann, J., Orlandi, F., Mchler, L., Vergniory, M. G., Sun, Y., Rost, A. W., Duppel, V., Krivenkov, M., Sheoran, S., Manuel, P., Varykhalov, A., Yan, B., Kremer, R. K., Ast, C. R. & Lotsch, B. V. Tunable Weyl and Dirac states in the nonsymmorphic compound CeSbTe. *Sci. Adv.* **4**, eaar2317 (2018).
5. Anand, V. K., Adroja, D. T., Bhattacharyya, A., Klemke, B. & Lake, B. Kondo lattice heavy fermion behavior in $\mathrm{CeRh_2Ga_2}$. *J. Phys. Condens. Matter* **29**, 135601 (2017).
6. Gignoux, D., Schmitt, D., Zerguine, M., Ayache, C. & Bonjour, E. Magnetic properties of a new Kondo lattice compound: $\mathrm{CePt_2Si_2}$. *Phys. Lett. A* **117**, 145–149 (1986).
7. Bhattacharjee, A., Coqblin, B., Raki, M., Forro, L., Ayache, C. & Schmitt, D. Anisotropy of transport properties in the Kondo compound $\mathrm{CePt_2Si_2}$: experiments and theory. *J. Phys. (Paris)* **50**, 2781–2793 (1989).
8. Dzsaber, S., Prochaska, L., Sidorenko, A., Eguchi, G., Svagera, R., Waas, M., Prokofiev, A., Si, Q. & Paschen, S. Kondo insulator to semimetal transformation tuned by spin-orbit coupling. *Phys. Rev. Lett.* **118**, 246601 (2017).
9. Nakamoto, G., Takabatake, T., Fujii, H., Minami, A., Maezawa, K., Oguro, I. & Menovsky, A. Crystal growth and characterization of the Kondo semimetal CeNiSn. *J. Phys. Soc. Jpn.* **64**, 4834–4840 (1995).
10. Kresse, G. & Hafner, J. Ab initio molecular dynamics for open-shell transition metals. *Phys. Rev. B* **48**, 13115–13118 (1993).
11. Kresse, G. & Furthmüller, J. Efficiency of ab-initio total energy calculations for metals and semiconductors using a plane-wave basis set. *Comput. Mater. Sci.* **6**, 15–50 (1996).
12. Perdew, J. P., Burke, K. & Ernzerhof, M. Generalized gradient approximation made simple. *Phys. Rev. Lett.* **77**, 3865–3868 (1996).
13. Kresse, G. & Joubert, D. From ultrasoft pseudopotentials to the projector augmented-wave method.

Phys. Rev. B **59**, 1758–1775 (1999).

14. Hobbs, D., Kresse, G. & Hafner, J. Fully unconstrained noncollinear magnetism within the projector augmented-wave method. *Phys. Rev. B* **62**, 11556–11570 (2000).

15. Nesterenko, S., Avzuragova, V., Tursina, A. & Kaczorowski, D. Structural peculiarities and magnetic properties of a novel cerium gallide $\mathrm{CeRh_2Ga_2}$. *J. Alloys Compd.* **717**, 136–140 (2017).

16. Herath, U., Tavadze, P., He, X., Bousquet, E., Singh, S., Muoz, F. & Romero, A. H. Pyprocar: A python library for electronic structure pre/post-processing. *Comput. Phys. Commun.* **251**, 107080 (2020).

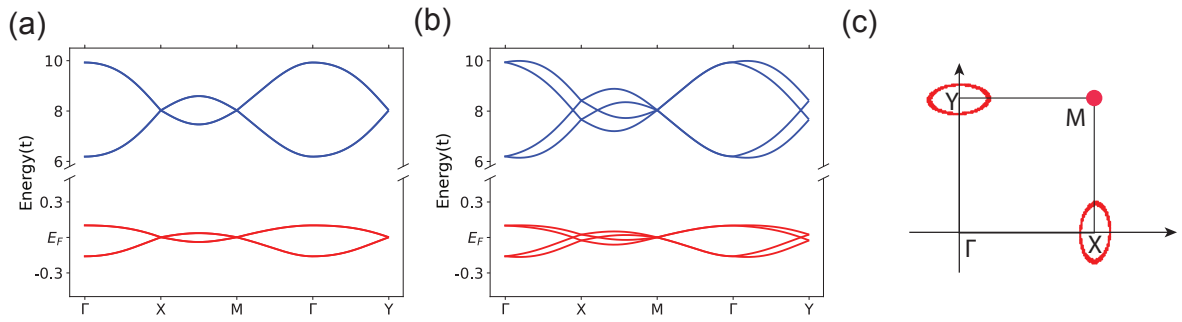

FIG. S1. **Kondo-driven composite fermions of a 2D square net. a,** The dispersion, including for the composite fermions (the lower red part), at $\Delta = 0$. The Kondo-driven Dirac nodes are pinned to E_F at the high-symmetry points X, Y, M. Here, the choice of parameters and the saddle-point analysis parallel those of Fig. 3(a). The input parameters are $(V, E_d, t_1, t_2, t^{SO}, \mu) = (6.8, -6, 1, 0, 0.6, -7.529)$. The saddle-point analysis yields $(r, l) = (0.285, -6.500)$. **b,** The dispersion of the Kondo-driven Weyl nodal-line semimetal. **c,** The Kondo-driven Weyl nodal lines (the red lines) encircle high symmetry points X and Y. Here $\Delta = 0.4$, and the other parameters are $(V, E_d, t_1, t_2, t^{SO}, \mu, r, l)$ = $(6.8, -6, 1, 0, 0.6, -7.564, 0.286, -6.500)$.

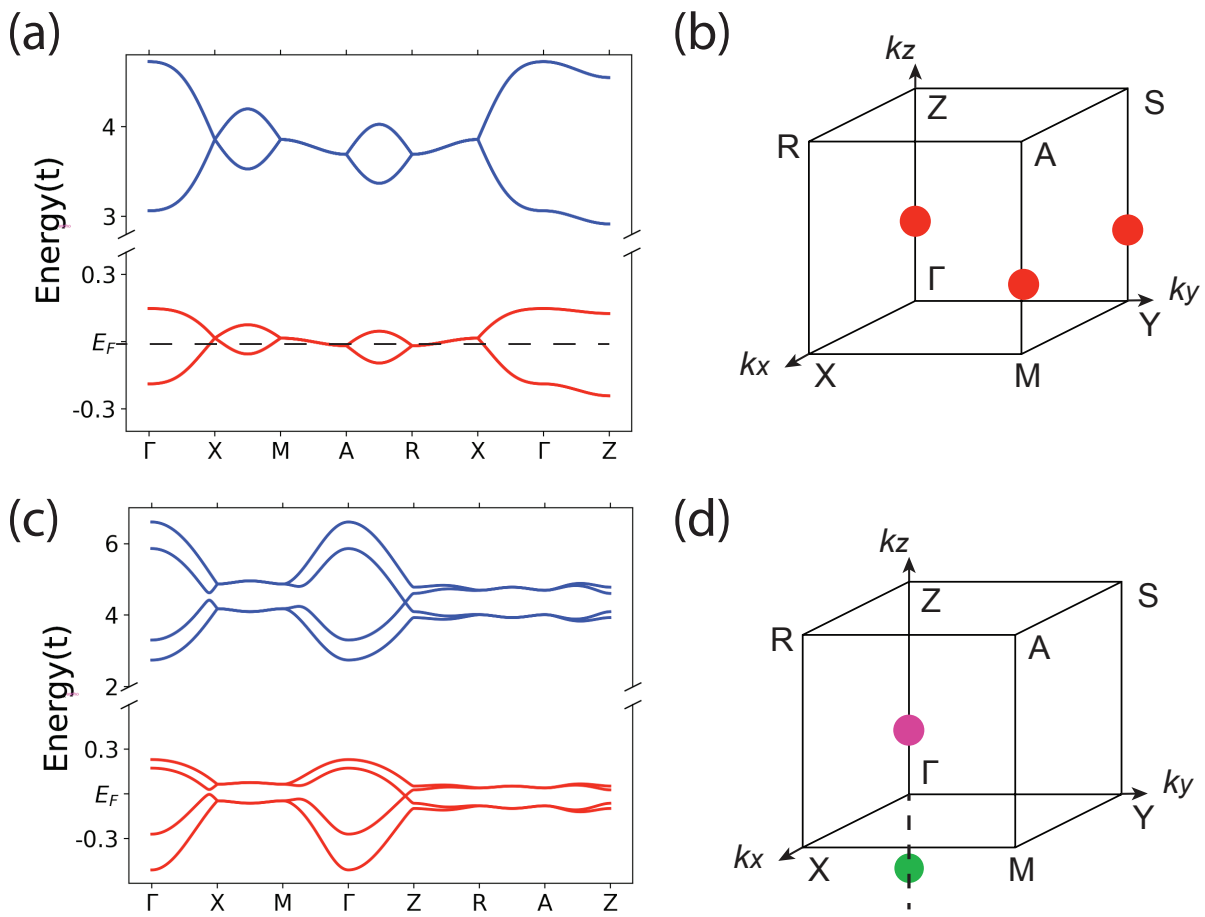

FIG. S2. **Kondo driven composite fermions in the 3D model for SG 129.** **a**, The dispersion, includes a symmetry enforced dispersive Dirac nodal line along $X - R$, $Y - S$ and $M - A$; and **b**, the points on the Dirac nodal line that cross the Fermi energy. The parameters for both **a** and **b** are $(t_1, t_2, t^{SO}, t_{1z}, t_{3z}, m_z, \Delta, V, E_d, \mu, r, l) = (1, 0, 0.4, 0.1, 0, 0, 0, 3.6, -2.6, -3.70, 0.44, -3.13)$; **c**, in the presence of a magnetic field, symmetry allows the existence of a pair of Weyl points along $\Gamma - Z$ as shown in **d**. The parameters are $(t_1, t_2, t^{SO}, t_{1z}, t_{3z}, m_z, \Delta, V, E_d, \mu, r, l) = (1, 0, 0.4, 0.1, 0.8, 0.3, 0, 3.6, -2.6, -3.82, 0.46, -3.53)$.

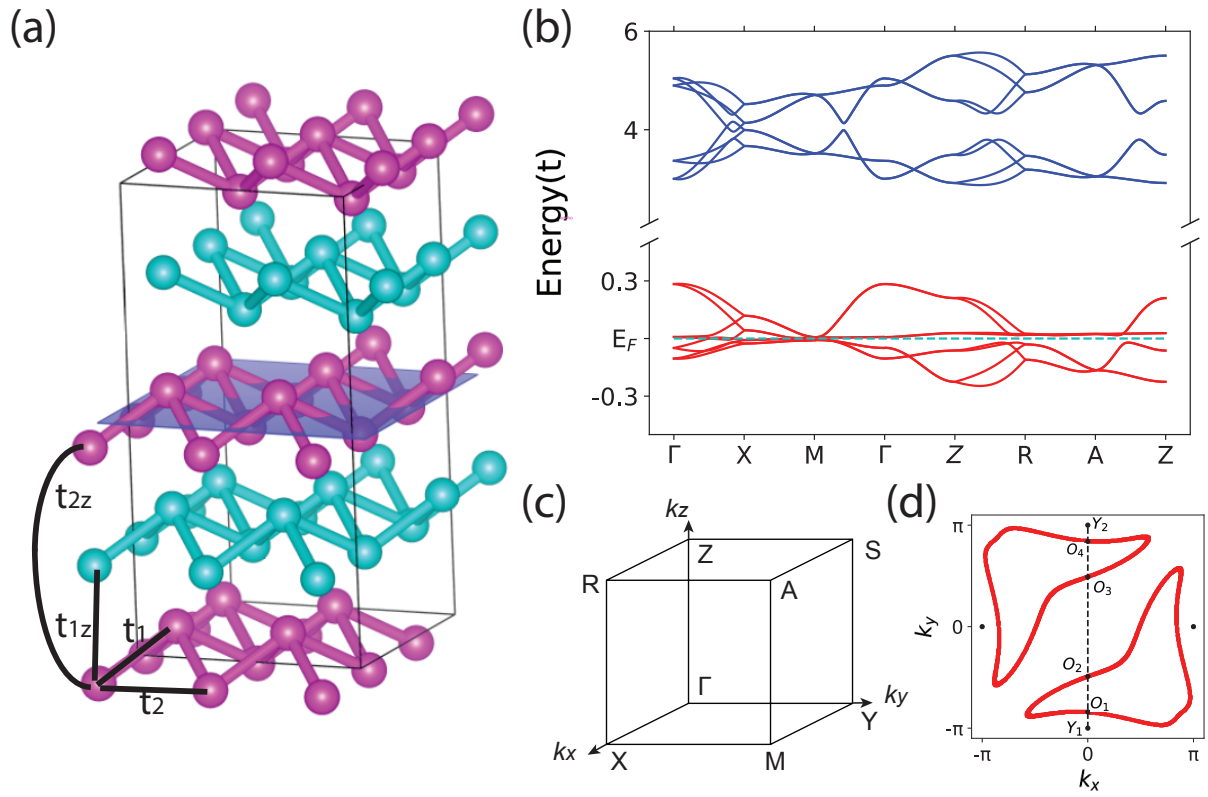

FIG. S3. **Kondo-driven composite fermions in the 3D model for SG 31 over an extended region of the Brillouin zone. a**, Illustration of the hopping parameters in the 3D-stacked model; **b,** The dispersion across both the $k_z = 0$ and $k_z = \pi$ planes with the same parameters as shown in Fig. 3. The composite fermions (lower red part) are fully gapped when $k_z \neq 0$. **c**, The 3D Brillouin zone with high symmetry points $\Gamma = (0, 0, 0)$, $X = (\pi, 0, 0)$, $Y = (0, \pi, 0)$, $M = (\pi, \pi, 0)$, $Z = (0, 0, \pi)$, $R = (\pi, 0, \pi)$, $S = (0, \pi, \pi)$ and $A = (\pi, \pi, \pi)$. **d,** The Kondo-driven Weyl nodal lines, which intersect with the dashed $k_x = 0$ line from $Y_1 = (0, -\pi, 0)$ to $Y_2 = (0, \pi, 0)$ at O_1, O_2, O_3 and O_4.

(a)

Space Group 129 with Ce at Wyckoff position 2c:
Candidate heavy fermion compounds that are not obviously metals, insulators, superconductors, or off-stoichiometric: 39

3 x 1-2: CeX_2 (*X*: S, Se, Te)

2 x 1-1-1: $CeSbX$ (*X*: Se, Te)

14 x 1-1-2: $CeTAs_2$ (*T*: Ni, Rh, Ag, Ir, Au), $CeTBi_2$ (*T*: Pd, Au), $CeTSb_2$ (*T*: Fe, Co, Ni, Cu, Pd, Ag, Au),

18 x 1-2-2: CeT_2Ga_2 (*T*: Rh, Pd), CeT_2Si_2 (*T*: Ir, Pt), CeT_2Ge_2 (*T*: Ir, Pt), CeT_2P_2 (*T*: Rh, Ir), CeT_2Sn_2 (*T*: Ni, Cu, Rh, Pd, Ir, Pt), $CeLi_2Sb_2$, CeT_2Sb_2 (*T*: Ni, Cu), $CeNi_2Bi_2$

1 x 1-1-3: $CePdSb_3$

1 x 2-3-5: $Ce_2Au_3Ga_5$

(b)

Space Group 31 with Ce:
$Ce_2Ni_7P_4$ – only structure determined
$Ce_2Au_3In_5$ – no magnetic order down to 2 K
$Ce_2Fe_{1.82}S_5$ – ferrimagnetic
$(NH_4)_5(Ce(NO_3)_2(H_2O)_3)(H_2W_{12}O_{40})(H_2O)_3$ – insulator

FIG. S4. **Further details in the search for correlation-driven topological semimetals.** Shown here are the materials identified during the intermediate step of the search procedure as outlined in Fig. 4(a) (main text) for SG 129 with Ce-ions on the Wyckoff position 2c (**a**) and in Fig. 4(b) (main text) for SG 31 with Ce atoms (**b**).

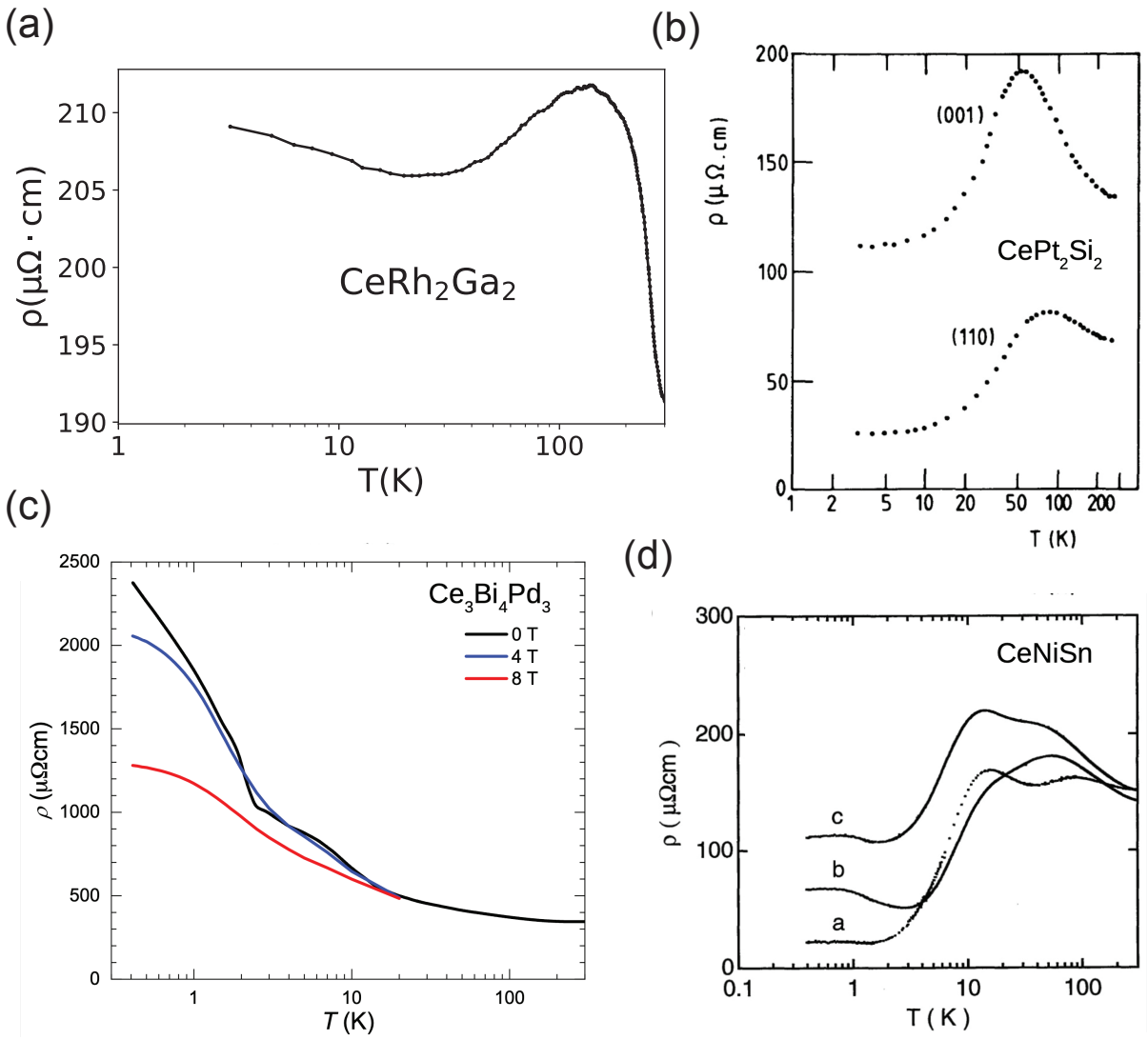

FIG. S5. **Semimetal transport of Ce-based square-net materials.** Resistivity (ρ) *vs.* temperature (T) of **a,** $CeRh_2Ga_2$ (replotted from Ref. 5), **b,** $CePt_2Si_2$[7], **c,** $Ce_3Bi_4Pd_3$[8], and **d,** $CeNiSn$[9]. All plots are shown in semi-log form.

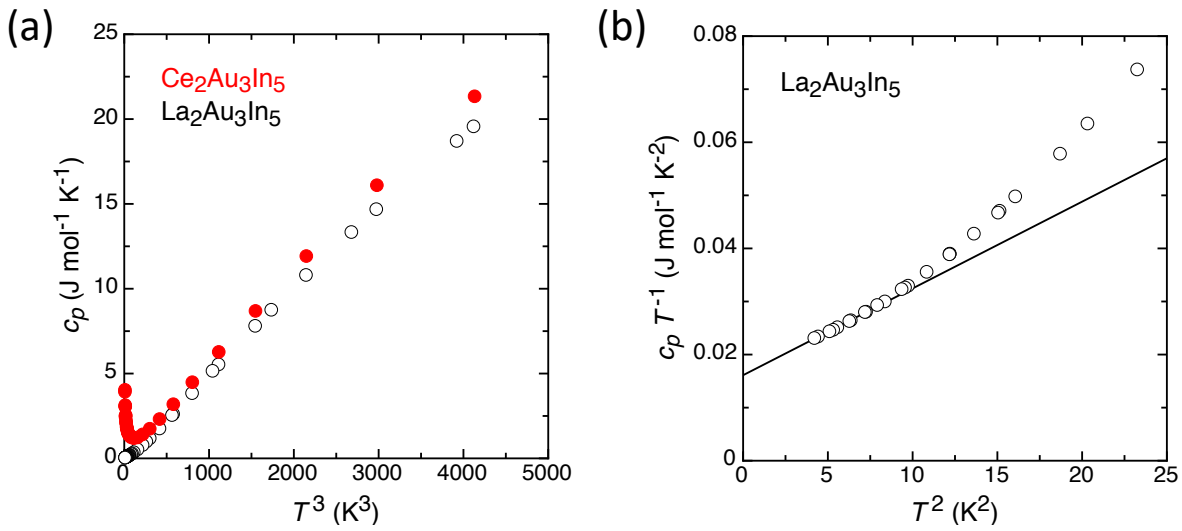

FIG. S6. **Specific heat of $Ce_2Au_3In_5$ and $La_2Au_3In_5$.** **a**, Total specific heat c_p as a function of T^3 for $Ce_2Au_3In_5$ (filled circles) and $La_2Au_3In_5$ (open circles). **b**, c_p/T of $La_2Au_3In_5$ as a function of T^2. The solid line is a Debye-Sommerfeld fit.

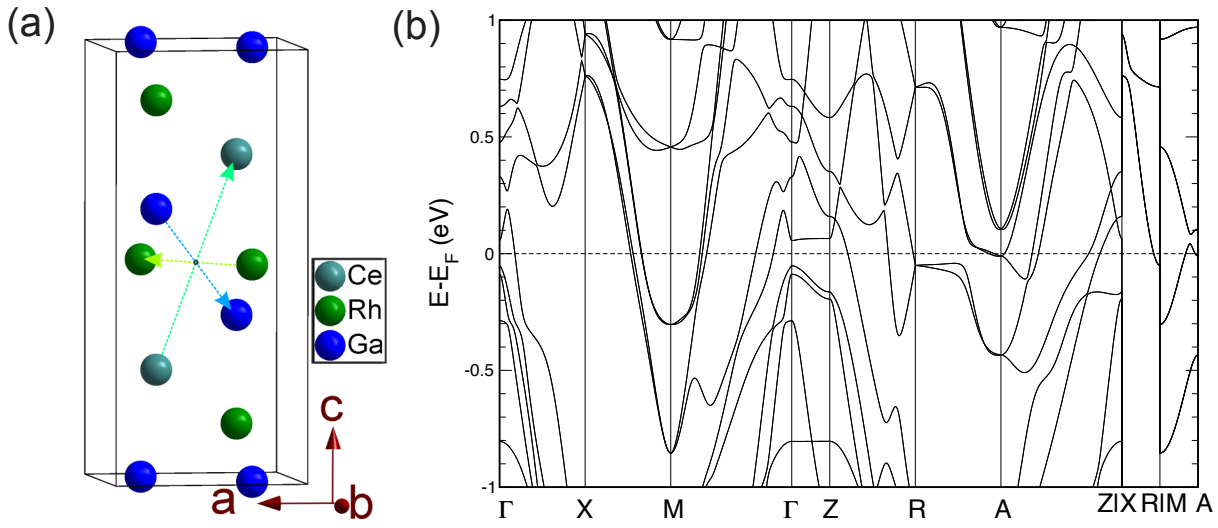

FIG. S7. **DFT results for** $CeRh_2Ga_2$**. a**, the crystal structure of $CeRh_2Ga_2$; **b**, the DFT results derived from ignoring the site-displacive disorder of the Rh and Ga atoms.

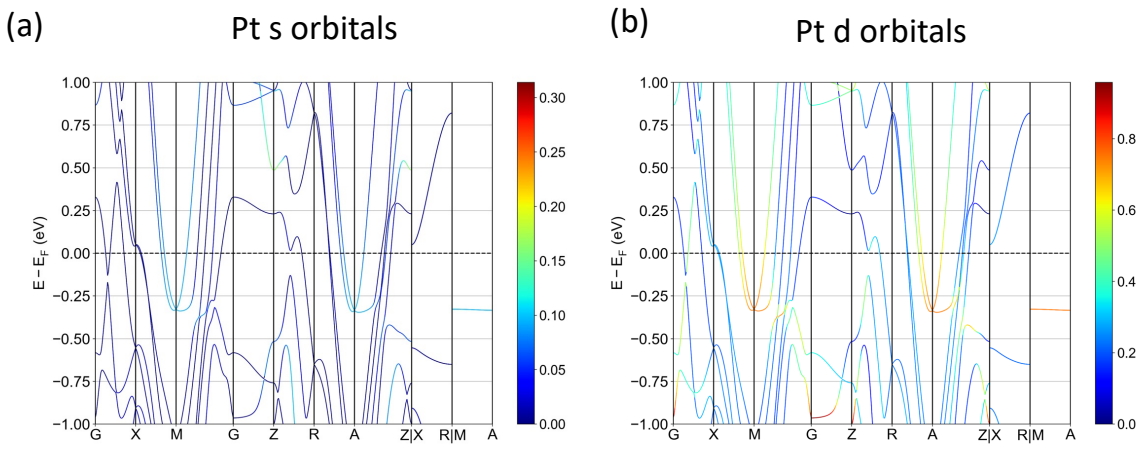

FIG. S8. **DFT results for the atomic and orbital contents of the** spd **conduction electrons in** $\mathbf{CePt_2Si_2}$**.** The dominating contributions are found to come from **a**, the Pt s-orbitals and **b**, the Pt d-orbitals. The bands have been plotted using PyProcar[16].